

See discussions, stats, and author profiles for this publication at: <https://www.researchgate.net/publication/228927570>

Zinc (II) Bisterpyridine Complexes: The Influence of the Cation on the π -Conjugation between Terpyridine and the Lateral Phenyl Substituent

ARTICLE in THE JOURNAL OF PHYSICAL CHEMISTRY C · OCTOBER 2008

Impact Factor: 4.77 · DOI: 10.1021/jp807461j

CITATIONS

30

READS

55

8 AUTHORS, INCLUDING:



Martin Presselt

26 PUBLICATIONS 365 CITATIONS

SEE PROFILE



Andreas Winter

Friedrich Schiller University Jena

98 PUBLICATIONS 2,103 CITATIONS

SEE PROFILE



Manuela Chipper

University of Strasbourg

22 PUBLICATIONS 450 CITATIONS

SEE PROFILE

Zinc(II) Bisterpyridine Complexes: The Influence of the Cation on the π -Conjugation between Terpyridine and the Lateral Phenyl Substituent

Martin Presselt,[†] Benjamin Dietzek,^{†,‡} Michael Schmitt,[†] Jürgen Popp,^{*,†,‡} Andreas Winter,[§] Manuela Chiper,[§] Christian Friebe,^{||} and Ulrich S. Schubert^{*,§,||}

Institute of Physical Chemistry, Friedrich-Schiller-University Jena, Helmholtz 4, 07743, Jena, Germany, Institute of Photonic Technology, Albert-Einstein-Str. 9, 07745 Jena, Germany, Laboratory of Macromolecular Chemistry and Nanoscience, Eindhoven University of Technology, P.O. Box 513, 5600 MB Eindhoven, The Netherlands, and Laboratory of Organic and Macromolecular Chemistry, Friedrich-Schiller-University Jena, Humboldtstr. 10, 07743 Jena, Germany

Received: August 20, 2008; Revised Manuscript Received: September 25, 2008

The synthesis and photophysical properties of an ethynylphenyl-substituted terpyridine ligand **L** and its corresponding zinc(II) complex $[\text{Zn}(\text{L})_2](\text{PF}_6)_2$, serving as model compounds for self-assembling Zn(II)-based metallopolymers suited for photoluminescent and electroluminescent devices, are presented. The UV–vis spectra are characterized, and the photoluminescence quantum yields are determined. The ground-state structures are calculated by means of DFT, and the structural key features are approved by experimental as well as by DFT-calculated Raman spectra. Special attention is paid to the π -electron delocalization between phenylene (ph) and pyridine (py) and, in particular, to changes in the ph–py bond due to complexation. The DFT-calculated ph–py bond shortening in $[\text{Zn}(\text{L})_2](\text{PF}_6)_2$ compared to **L** correlates well with the higher wavenumber of the $\nu(\text{ph}–\text{py}(\text{trig}))$ vibration, which involves strong ph–py bond stretching. The higher ellipticity in the ph–py bond due to complexation, calculated according to Bader's QTAIM indicating the π -character of a bond, is confirmed by the higher Raman intensity of the $\nu(\text{ph}–\text{py}(\text{trig}))$ vibration. The electron density distributions in the ph–py bond between $[\text{Zn}(\text{L})_2](\text{PF}_6)_2$ and **L** are compared in an *inter*– $\Delta\rho$ plot, which highlights the changes in the bonding situation of the ph–py bond induced by complex forming.

Introduction

The self-assembly of coordinating ligands by metal ion complexation to highly ordered architectures is a common approach in modern supramolecular chemistry.¹ In particular, oligopyridine compounds, featuring remarkably high binding affinity toward most transition metal ions by $d\pi \rightarrow p\pi^*$ bonding and good chelating properties, have widely been used as building blocks in this context.² Notably, 2,2':6',2''-terpyridines bearing π -conjugated substituents at the 4'-position show interesting photophysical and electrochemical properties with respect to potential applications in the fields of self-assembled molecular devices and photoactive molecular wires.^{2–4} The photophysical properties of the organic ligands can easily be tuned by the complexation with suitable transition metal ions and the attachment of functional groups or polymer chains.⁵ Electronic communication between metal-complexed units of bis- and tris(terpyridine)s is another fascinating feature highlighting their potential in the design of new functional materials.⁶ Besides heavy transition metal ions—such as Ru(II), Os(II), or Ir(III)—Zn(II) has gained much interest as templates for the construction of photoluminescent (PL) or electroluminescent (EL) metallopolymers with well-defined structures.⁷ Depending on the nature

of the π -conjugated system between the terpyridine units, emission properties can be tuned, and materials with high PL quantum yields and EL performance are accessible. Recently, analogous Zn(II)-based grafted structures^{8a} as well as hexameric metallocycles^{8b} have also been reported. It is well-known from the literature that metal-to-ligand charge transfer (MLCT) processes do not occur for metal ions with filled electron shells, such as Zn(II) with its d^{10} configuration.⁹ Hence, only *intraligand* (IL) charge transfer is observed between terpyridine–zinc(II) units and the chromophores, even in metallo-polymers.¹⁰ Thus, the development of Zn(II)-containing metallo-polymers with well-designed chromophores or π -conjugated spacers can lead the way toward high-performance emissive host materials in PLED applications.

Herein, we present the synthesis of a Zn(II) bisterpyridine complex as a model substrate for analogous Zn(II)-based metallo-polymers. A detailed study on the influence of the complexation on the photophysical properties of the corresponding ligand is performed. Representatively, we have chosen 4'(4-ethynylphenyl)-2,2':6',2''-terpyridine (**L**) and its corresponding zinc(II) complex $[\text{Zn}(\text{L})_2](\text{PF}_6)_2$ out of a series of differently phenyl-substituted terpyridine derivatives to investigate the changes in the UV–vis absorption behavior, geometrical structure, Raman spectrum, and electron density distribution due to complexation. Thereby, we detail the electronic and geometrical structure of the ph–py bond to unravel the influence of the complexation on π -electron delocalization between the terpyridine and the phenylene moiety. The delocalization is correlated with the torsion of the aromatic systems against each other, as pointed out in recently published studies.¹¹ For the study of the π -electron delocalization between terpyridine and

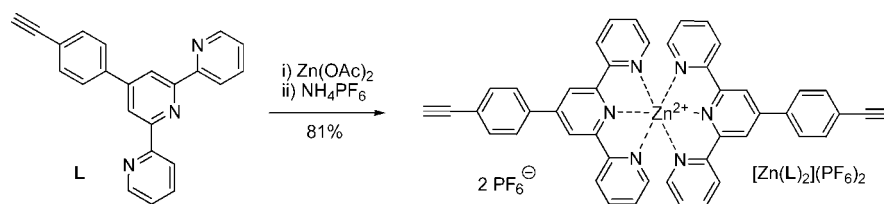
* To whom correspondence should be addressed. Synthesis, NMR spectroscopy, absorption/fluorescence spectroscopy (U.S.S.) Phone: (+49)(0)3641 948202. E-mail: ulrich.schubert@uni-jena.de. Raman spectroscopy, theoretical calculations (J.P.). Phone: (+49)(0)3641 948320. E-mail: juergen.popp@uni-jena.de.

[†] Institute of Physical Chemistry, Friedrich-Schiller-University Jena.

[‡] Institute of Photonic Technology.

[§] Eindhoven University of Technology.

^{||} Laboratory of Organic and Macromolecular Chemistry, Friedrich-Schiller-University Jena.

SCHEME 1: Schematic Representation of the Synthesis of the Complex $[\text{Zn}(\text{L})_2](\text{PF}_6)_2$ 

phenylene, we applied Bader's QTAIM.^{12a,13} Finally, we generated an intermolecular electron-density-difference plot (*inter*- $\Delta\rho$ plot), to compare the electron density distribution of a particular common substructure between two different molecules. In this way, changes in the ph-py bond due to complexation can be highlighted. Such visualization techniques are rarely applied in the context of comparing bonding situations between different molecules.^{14,15} However, in this study, the potential of the *inter*- $\Delta\rho$ plot to gain insights into the effect of structural changes on bonding situations is presented.

Experimental Section

Materials and General Experimental Details. All chemicals were of reagent grade, purchased from Aldrich, Acros, and ABCR, and used as received unless otherwise specified. The solvents were obtained from Biosolve and dried according to literature procedures. 4'-(4-Ethynylphenyl)-2,2':6',2''-terpyridine (**L**) was synthesized as previously published.^{4g}

Instrumentation. ¹H NMR spectra were recorded at 25 °C on a Varian Mercury 400 MHz instrument using CDCl₃ and CD₃CN as solvents and TMS as an internal standard. Matrix-assisted laser desorption-ionization time-of-flight mass spectrometry (MALDI-TOF MS) was performed on a Voyager-DE PRO biospectrometry workstation (Applied Biosystems) time-of-flight mass spectrometer, with dithranol as matrix. UV/vis absorption spectra were measured on a Perkin-Elmer Lambda-45 spectrometer. Fluorescence spectra were recorded on a Perkin-Elmer LS50B luminescence spectrometer. Absolute phosphorescence quantum yields in dilute solution were determined on a Hamamatsu C9920-02 QY system. For these three techniques, 10⁻⁶ M solutions in CH₂Cl₂ were used. Elemental analysis was obtained on a Euro Vector EuroEA3000 elemental analyzer for CHNS-O. Raman spectra of solid samples were recorded with a Jobin Yvon Labram HR-spectrometer, equipped with an Olympus BX41 inverse microscope. The 830 nm output from a diode laser was used as a Raman excitation source, and the scattered light was detected with a CCD detector. A grating with 300 grooves/mm was applied leading to a spectral resolution of roughly 1 cm⁻¹.

DFT Calculations and AIM Studies. DFT calculations were carried out employing the program Turbomole.¹⁶ The pure density functional of Becke and Perdew BP86 and the triple- ξ TZVP basis set (polarization function on all atoms) were used.¹⁷⁻¹⁹ This Ahlrich-type basis set consists of 5s1p functions contracted to 3s1p for H (according to scheme [311/1]) and 11s6p1d functions contracted to 5s3p according to [62111/411/1] for B to Ne. For all calculations, the resolution-of-the-identity (RI) technique was applied.²⁰ For the frequency analysis, the program package SNF was used.²¹ The obtained wavenumbers of the vibrational normal modes were not adjusted to experimental values by applying scaling factors. Electron density plots were generated employing Turbomoles *pointval* option and Mathematica for visualization.²² Electron density features according to Bader's QTAIM were calculated using the AIM2000

program. The corresponding wave function files were produced using the molden2wfn tool.¹²

Synthesis of $[\text{Zn}(\text{L})_2](\text{PF}_6)_2$. To a solution of 4'-(4-ethynylphenyl)-2,2':6',2''-terpyridine (**L**, 1 mmol) in abs. methanol (100 mL), a solution of Zn(OAc)₂·2H₂O (0.5 mmol) in abs. methanol (30 mL) was added. After stirring at room temperature for 3 h, an excess of NH₄PF₆ was added. The precipitate was filtered off and washed successively with methanol (3 × 20 mL), water (2 × 20 mL), and diethyl ether (2 × 20 mL). Further purification of the crude product was achieved by recrystallization from acetonitrile/diethyl ether. The complex was finally dried under vacuum at 40 °C for 24 h.²³ Yield: 81%. ¹H NMR (400 MHz, CD₃CN): δ 8.90 (s, 4 H, 3',5'-*H*_{tpy}), 8.73 (d, ³*J* = 8.0 Hz, 4 H, 3,3''-*H*_{tpy}), 8.26–8.17 (m, 8 H, 4',4''-*H*_{tpy} & *H*_{aryl}), 7.89 (d, ³*J* = 8.5 Hz, 4 H, *H*_{aryl}), 7.85 (d, ³*J* = 4.9 Hz, 6,6''-*H*_{tpy}), 7.43 (m_c, 4 H, 5',5''-*H*_{tpy}), 3.70 (s, 1 H, *H*_{ethynyl}) ppm. MALDI-TOF MS (dithranol): *m/z* = 875.15 ([*M* - PF₆]⁺). Anal. Calcd for C₄₆H₃₀F₁₂N₆P₂Zn: C, 54.06; H, 2.96; N, 8.22. Found: C, 54.32; H, 3.17; N, 8.05.

Results and Discussion

Synthesis and Characterization. The Zn(II) complex investigated herein is based on a 2,2':6',2''-terpyridine ligand bearing a π -conjugated substituent in the 4'-position. Terpyridine derivative **L** has been synthesized conveniently applying a previously published one-pot procedure.^{4g} The nature of the thusly prepared ligand has been confirmed by NMR spectroscopy, MALDI-TOF mass spectrometry, and elemental analysis. The corresponding homoleptic Zn(II) bisterpyridine complex $[\text{Zn}(\text{L})_2](\text{PF}_6)_2$ has been obtained in high yields (81% after recrystallization from acetonitrile/diethyl ether) by reacting terpyridine **L** with zinc acetate at a ratio of 2:1 in methanol at ambient conditions, followed by subsequent anion exchange with ammonium hexafluorophosphate (Scheme 1).²⁰ The ¹H NMR spectrum of the complex, as recorded in CD₃CN, has revealed well-resolved signals in the aromatic region. In comparison to the free ligand **L**, the *H*^{3',5'}, *H*^{3,3''}, *H*^{4,4''}, and *H*^{5,5''} signals of the terpyridyl units have shown a distinct downfield shift. Due to the octahedral geometry of the complex, the protons in the 6,6''-position are directed toward the shielding region of the central pyridine ring of the orthogonal neighboring ligand resulting in some considerable upfield shielding of these signals.²⁴ The ¹H NMR spectra of the ethynyl-substituted terpyridine **L** and the corresponding complex $[\text{Zn}(\text{L})_2](\text{PF}_6)_2$ are depicted in Figure 1.

Photophysical Properties. After approving the structural constitution of ligand **L** and the corresponding zinc complex $[\text{Zn}(\text{L})_2](\text{PF}_6)_2$ the photophysical properties as determined by UV/vis absorption and photoluminescence spectroscopy of dilute solutions will be discussed. The photophysical characteristics are summarized in Table 1.

A comparison between the UV-vis spectra obtained for the free ligand **L** and the derived zinc complex $[\text{Zn}(\text{L})_2](\text{PF}_6)_2$ is shown in Figure 2. In general, two major absorption regions

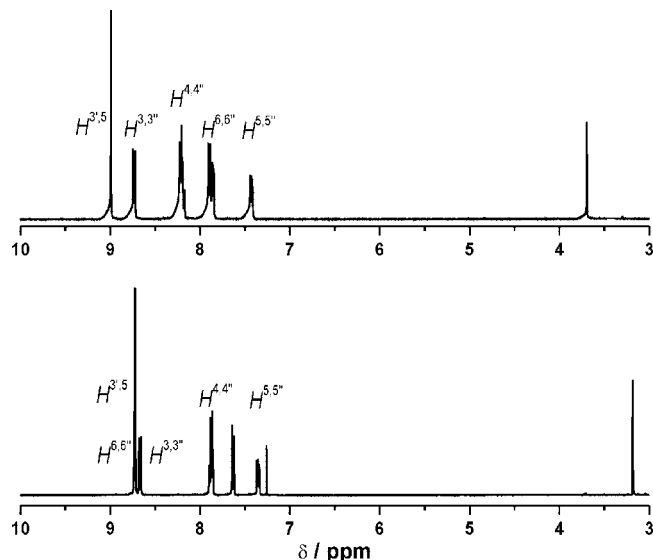


Figure 1. ^1H NMR spectra (400 MHz, room temperature) of terpyridine **L** (top, in CDCl_3) and $[\text{Zn}(\text{L})_2](\text{PF}_6)_2$ (bottom, in CD_3CN).

TABLE 1: Photophysical Properties of **L and $[\text{Zn}(\text{L})_2](\text{PF}_6)_2$**

entry	$\lambda_{\text{abs,max}}/\text{nm}^a$	$E_{\text{g}}^{\text{opt}}/\text{eV}^b$	$\lambda_{\text{PL,max}}/\text{nm}^a$	$\lambda_{\text{S}}/\text{nm}$	Φ_{PL}^a
L	282	3.14	362	80	0.61
$[\text{Zn}(\text{L})_2](\text{PF}_6)_2$	284	3.60	427	143	0.34

^a Absorption and photoluminescence spectra ($\lambda_{\text{abs,max}}$, $\lambda_{\text{PL,max}}$ are the positions of the maxima, λ_{S} is the Stokes shift) as well as absolute quantum efficiencies Φ_{PL} have been measured in dilute CH_2Cl_2 solutions (10^{-6} M for all compounds). ^b Optical band gaps $E_{\text{g}}^{\text{opt}}$ have been estimated from the absorption spectra at 10% absorption on the longer wavelength side.

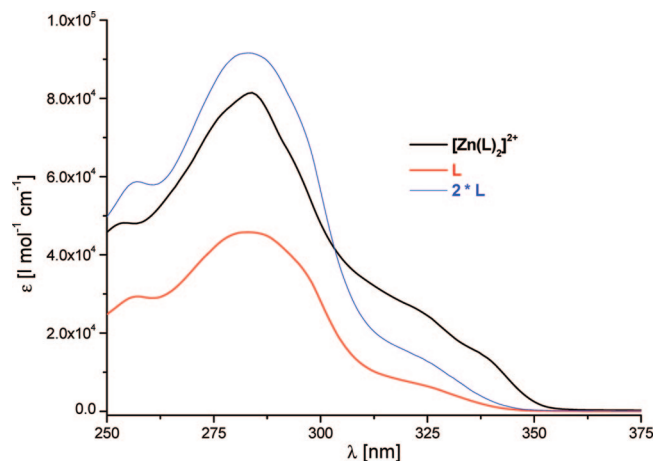


Figure 2. UV-vis spectra of **L** and the corresponding zinc(II) complex $[\text{Zn}(\text{L})_2](\text{PF}_6)_2$. In addition, the UV-vis spectrum of **L** multiplied by two, to allow the comparison between the UV-vis spectra of **L** and $[\text{Zn}(\text{L})_2](\text{PF}_6)_2$, is included.

have been observed. In either system, the band between 280 and 295 nm belongs to the terpyridine unit,²⁵ while the bands between 310 and 350 nm are assigned to phenylene-localized transitions. Generally, the UV-vis spectrum of $[\text{Zn}(\text{L})_2](\text{PF}_6)_2$ reveals nearly twice the extinction of the UV-vis spectrum of **L** since $[\text{Zn}(\text{L})_2](\text{PF}_6)_2$ possesses two of the ligands **L** with the respective chromophor systems.

In the UV-vis spectrum of $[\text{Zn}(\text{L})_2](\text{PF}_6)_2$, the region between 310 and 350 nm shows two bands at 325 and 340 nm, whereas the latter is not visible in the UV-vis spectrum of **L** (Figure 2). The UV-vis spectrum of **L** has been multiplied with

a factor of 2 to highlight the shift of the bathochrome absorption edge of $[\text{Zn}(\text{L})_2](\text{PF}_6)_2$ to lower energies compared to the respective band of **L**. This bathochromic shift might be due to a shift of a phenylene-based transition to lower energies or the absorption increase of a bathochrome phenyl transition due to complexation. In both cases, the shift is attributed to a change in the π -system of the phenylene moiety. This change is expected to be rather a slight extension of the ph- π system along the ph-py bond than along the ethynyl group since the latter should remain unaffected by the complex formation.

Even if the supposed slight change of the ph-py- π character is located close to the tpy-chromophor system, a significant bathochrome shift of the low-energy tpy-absorption edge is neither expected nor observed in Figure 2. This is due to the assignment of a low-energy tpy-absorption (bathochrome edge of the absorption band around 280 nm) to the tpy-long-axis transition with a transition moment perpendicular to the ph-py bond. The tpy-long-axis transition is expected to be of lower energy and of lower oscillator strength than the transition corresponding to the short tpy axis.²⁵ Since the transition dipole moment of the tpy-short-axis transition is parallel to the ph-py bond, it should be influenced somewhat more by the higher π -character in the ph-py bond. However, a significant corresponding bathochromic shift is not observable in the hypsochromic edge of the tpy-assigned absorption band (280–295 nm) of $[\text{Zn}(\text{L})_2]^{2+}$ compared to **L** (Figure 2). That means that even if the π -character of the ph-py bond is somehow increased due to complexation neither of the energies of the tpy-located electronic transitions is significantly lowered.

Structural Characterization and Examination of the Electron Density Distribution using DFT and Raman Spectroscopy. Assuming a change in the electron density (ρ) distribution within **L** upon complexation to be responsible for the bathochromic shift in the phenyl-absorption band around 340 nm, we studied how this change in the ρ -distribution can be correlated with changes in the DFT-calculated geometries. To experimentally corroborate structural changes and changes in the π -electron delocalization due to complexation, Raman spectroscopic experiments were performed. The differences in the topology of the ρ -distribution in the ph-py bond between **L** and $[\text{Zn}(\text{L})_2]^{2+}$ have been analyzed utilizing Bader's QTAIM and were correlated with changes of particular Raman data. To extend the comparison of the ρ -distribution of a particular common substructure between two different molecules beyond single points, a novel technique for visualization according to the work of Grier et al. and others¹⁵ of the ρ -differences is presented.

Characterizing Ligand **L via DFT-Optimized Geometries and Raman Spectra.** Before being able to compare DFT-calculated geometrical differences and differences in the Raman spectra between **L** and $[\text{Zn}(\text{L})_2]^{2+}$, the structure and Raman spectrum of **L** has to be discussed. The geometry optimizations with subsequent calculations of the Raman spectra of various conformers of the free ligand and of the zinc complex were performed using the BP86 functional and the TZVP basis set.^{17–19} This combination has shown to provide accurate molecular structures, frequencies, and Raman intensities for medium-sized molecules.^{26,27}

While calculating the experimental Raman spectrum of **L**, one has to account for the different conformers of **L**. The two most important conformers are the all-*cis* and the all-*trans* structures with respect to the terpyridine moiety. This is because the orientation of the terminal pyridines in the all-*cis* conformer is somehow comparable to the situation in the complex, while

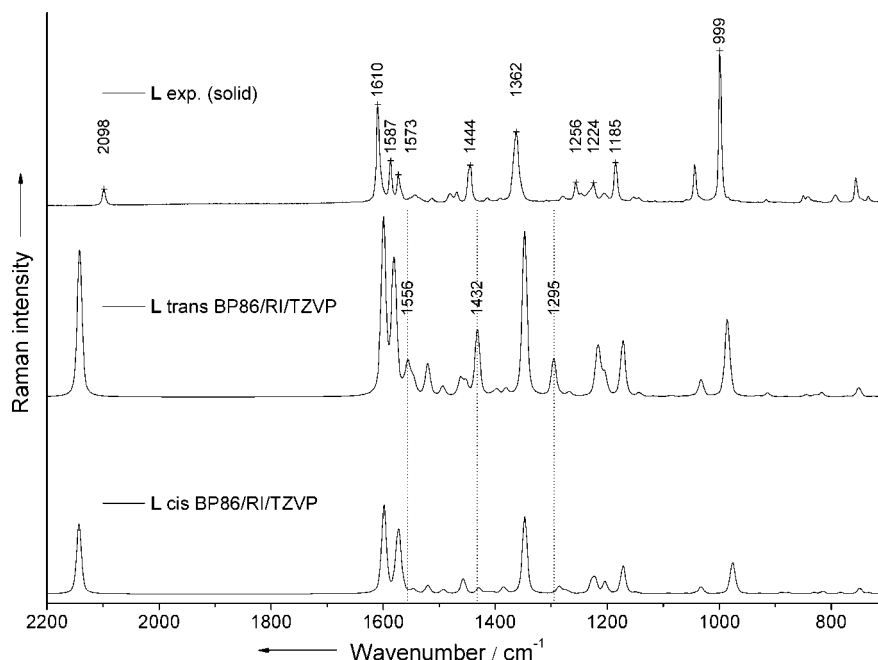


Figure 3. Raman spectra of **L**. Top: Experimental RS ($\lambda_{\text{ex}} = 830$ nm; grating: 300 gr/mm, solid sample). Middle and bottom: DFT calculated RS of all-*trans*-**L** and all-*cis*-**L** (functional: BP86, basis-set: TZVP, RI-approximation).

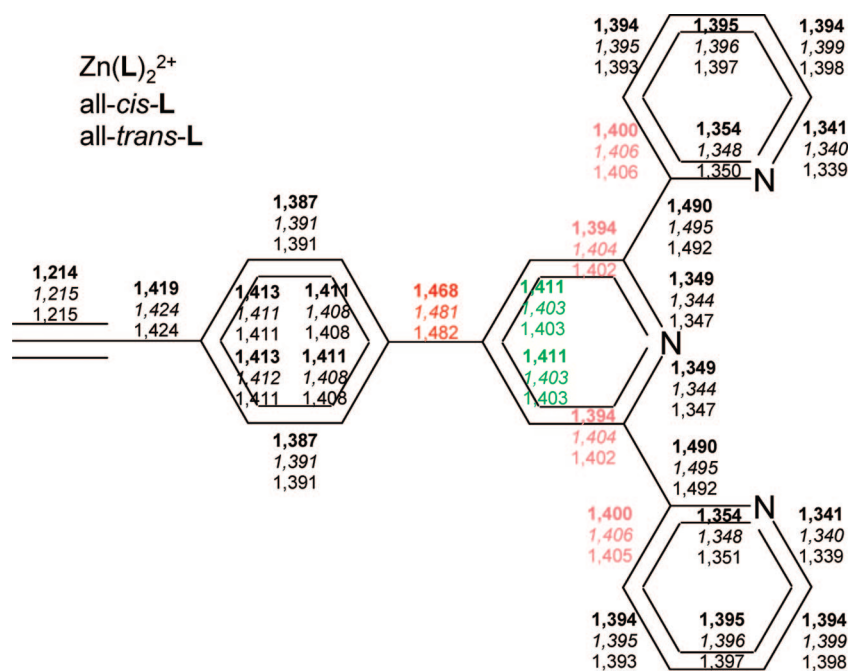


Figure 4. Bond lengths in the ligand **L** and the corresponding complex $[\text{Zn}(\text{L})_2](\text{PF}_6)_2$ as derived from DFT calculations. Significant changes upon complexation: pale red, 0.006–0.01 Å shortened bonds; red, >0.01 Å shortened bond; green, >0.006 Å elongated bonds.

the all-*trans* conformer is expected to correspond to the global energetic minimum of the free ligand. The electronic energy of the all-*trans* conformer has been calculated to be -1050.065 h, and the Gibbs enthalpy is 670.78 kJ/mol. The electronic energy of the all-*cis* conformer is about 0.02 h higher (-1050.045 h), and the corresponding Gibbs enthalpy is about 3 kJ/mol lower (667.94 kJ/mol) than for the all-*trans* conformer. Errors of these DFT energies have been estimated to be below 0.1 mh/atom.²⁰ This allows the estimation of the accuracy of computed energies of the **L** conformers (83 atoms) to be about 0.008 h. The most obvious differences in geometry of the two conformers are the dihedral angles between the aromatic rings. Geometry optimization of the all-*trans* conformer confirmed the expected planar structure in the terpyridine unit with the

phenylene group being tilted about 33.2° out-of-plane. This dihedral angle was calculated to be about 3° larger (36.5°) in the case of the all-*cis* conformer, while the angle between the pyridine rings is about 41° . The bond length of the ph–py bond differs negligibly between the all-*cis* and the all-*trans* conformer, which is shown in Figure 4 in the next section in context with the influence of the complexation.

In Figure 3, the experimental Raman spectrum of **L** is compared to the DFT-calculated Raman spectra of the all-*cis* and the all-*trans* conformer of **L**. The most intense bands are at comparable wavenumber positions with an equivalent intensity pattern. In the DFT calculated Raman spectra of **L**, the intense band at 980 cm^{-1} can be assigned to trigonal ring breathing vibrations located in the terpyridine moiety with

TABLE 2: Selected Parameters Indicating Variations in the π -Electron Delocalization Due to Complexation

compound	α^{a}	$r(\text{py}_c\text{-ph})/\text{\AA}^b$	wavenumber/ cm^{-1c}		Raman c,d		BCP($\text{py}_c\text{-ph}$)	
	DFT	DFT	DFT	exp.	activity/ $\text{\AA}^4/\text{amu}$	int. ratio	$\rho_b/\text{e}/\text{\AA}^3$	ϵ_b
<i>cis</i> - L	36.5	1.481	1347.2	1362	1400	0.772	0.255	0.069
<i>trans</i> - L	33.2	1.482	1347.5		1692		0.260	0.058
$[\text{Zn}(\text{L})_2]^{2+}$	30.0	1.468	1351.4	1370	6171	1.345	0.255	0.081

^a Dihedral angle between the central pyridine ring and the phenyl substituent (py–ph). ^b Bond length between the central pyridine ring and the phenyl substituent. ^c $\nu(\text{ph-py}(\text{trig}))$. ^d Raman activity: DFT calculated; Raman intensity ratio: experimentally determined, $\nu(\text{ph-py}(\text{trig. ring br.}))$.

quasistationary carbon atoms forming the inter aromatic ring bonds. The band at 1347 cm^{-1} is assigned to a trigonal ring breathing vibration basically located on the central pyridine ring and the phenylene unit. It involves strong movements of the interaromatic-ring-bond carbon atoms, which are accompanied by a pronounced stretch vibration of the phenylene and pyridine connecting bond (C–(H) and N in the central py quasistationary). The bands at 1575 and 1600 cm^{-1} are assigned to aromatic in-plane vibrations corresponding to Wilson No. 8a, located either in the terpyridine unit (1575 cm^{-1}) or in the phenylene group (1600 cm^{-1}).²⁸ Finally, the Raman band at 2142 cm^{-1} corresponds to the well-separated stretching vibration of the ethynyl group. These modes can be easily identified in the experimental Raman spectrum (RS) of the free ligand **L** (Figure 3). The DFT calculated modes at 980 , 1647 , 1575 , 1600 , and 2142 cm^{-1} correspond to bands at 999 , 1362 , 1587 , 1610 , and 2098 cm^{-1} in the experimental RS. The somewhat modified intensity pattern in the experimental RS compared to the DFT calculated one is due to a lower spectrometer sensitivity at higher wavenumbers applying an 830 nm laser line for excitation. The good agreement between experimental and DFT calculated Raman spectra suggests that the structural features obtained from the DFT calculations are reasonable.

The differences between the DFT-calculated Raman spectra of all-*cis*- and all-*trans*-**L** allow us to determine which of the conformers, primary differing in dihedral angles between the pyridine rings, is present in the experiment. Monitoring the differences in the dihedral angles directly by Raman spectroscopy appears rather challenging because the corresponding torsional modes are expected to occur in the low wavenumber region with strongly reduced Raman intensities. However, differences of the dihedral angles between the aromatic rings influence the aromatic in-plane vibrational modes that dominate the Raman spectrum in the region between 900 and 1700 cm^{-1} . In particular, the rather intense Raman bands calculated to occur at 1296 , 1433 , and 1556 cm^{-1} in the spectrum of the all-*trans* conformer are not clearly identifiable in the corresponding Raman spectrum of the all-*cis* conformer. Hence, they appear to be appropriate marker bands for the *trans* conformation. Experimentally, these marker bands are observed at 1444 and 1573 cm^{-1} . Though, the calculated marker band of the *trans*-**L** at 1296 cm^{-1} cannot be clearly identified in the experimental data, the strong presence of the other *trans*-characteristic bands in the experimental spectrum of **L** suggest that the latter spectrum is mainly dominated by the *trans* conformer.

Investigation of the Changes in Geometry upon Complexation and Discussion of the Raman Spectrum of $[\text{Zn}(\text{L})_2]^{2+}$. According to the DFT calculations, the terpyridine moiety in $[\text{Zn}(\text{L})_2](\text{PF}_6)_2$ is planar in contrast to the free *cis*-**L**. Consequently, the larger overlap of the free electron pairs of the nitrogen atoms with the d-orbitals of the zinc(II) ion in combination with a higher degree of π -delocalization in the planar terpyridine moiety compensates the steric hindrance of

the neighboring hydrogen atoms on the respective pyridines. Furthermore, the dihedral angle between the phenylene and pyridine rings is with 30.0° slightly but distinctly lower than in both conformers of the uncomplexed ligand as shown in Table 2 (*cis*-**L**: 36.5° , *trans*-**L**: 33.2°).

The DFT calculations reveal that most of the carbon–carbon bond lengths differ less than 0.005 \AA between the uncomplexed **L** and $[\text{Zn}(\text{L})_2](\text{PF}_6)_2$ (Figure 4). However, bonds that are shortened due to complexation are the pyridine–carbon–carbon bonds adjacent to the pyridine connecting bonds. The respective bond lengths differ from 0.006 to 0.01 \AA (0.4 – 0.7%) between $[\text{Zn}(\text{L})_2](\text{PF}_6)_2$ and any of the conformers of **L** and are colored pale red in Figure 4. The most significant shortened bond due to complexation is the ph–py bond with a length of 1.468 \AA in $[\text{Zn}(\text{L})_2](\text{PF}_6)_2$ compared to 1.481 and 1.482 \AA in all-*cis*-**L** and all-*trans*-**L**, respectively (Figure 4, red labels). Besides the bond shortening, significant bond elongations of 0.008 \AA (0.6%) are observed for pyridine–carbon–carbon bonds adjacent to the ph–py bond (Figure 4, green labels).

The value of the dihedral angle between phenyl and pyridine is lowered upon complexation. Concertedly, the ph–py bond is shortened indicating a higher degree of π -delocalization between ph and py in $[\text{Zn}(\text{L})_2](\text{PF}_6)_2$ compared to free **L**. The lower dihedral angle goes along with a larger overlap of the π -orbitals of the carbon atoms of the ph–py bond. Additionally, the shortening of the ph–py bond indicates a higher bond order and with it also a higher π -character of the ph–py bond.

By comparing the Raman spectra of **L** and $[\text{Zn}(\text{L})_2]^{2+}$, it can be seen that the most intense Raman bands appear at comparable wavenumbers and with comparable relative Raman intensities (Figure 5). Hence, the vibrational pictures of $[\text{Zn}(\text{L})_2]^{2+}$ underlying these intense bands, e.g., the aromatic in plane vibrations, are comparable to those of **L**, described in the previous section. Identical or energetically closely spaced vibrations on both ligands in $[\text{Zn}(\text{L})_2]^{2+}$ are coupled. This coupling leads to a splitting of **L**-modes giving rise to symmetrical and 180° phase shifted modes in $[\text{Zn}(\text{L})_2]^{2+}$, slightly shifted to higher or lower wavenumbers. Hence, differences in the Raman spectra, e.g., the vibration corresponding to the band at 1362 cm^{-1} in the Raman spectrum of **L** (see Figure 3) assigned to the band at 1370 cm^{-1} in the Raman spectrum of $[\text{Zn}(\text{L})_2]^{2+}$ (Figure 5, Table 2), are due to geometrical changes upon complexation and slight shifts caused by mode-coupling in $[\text{Zn}(\text{L})_2]^{2+}$ to some extent (see the Supporting Information for complete vibrational assignment, supported by a DFT calculated Raman spectrum). The DFT-calculated Raman spectrum is in good agreement with the experimental Raman spectrum (see Figure 5) and is based on the fully optimized geometry of $[\text{Zn}(\text{L})_2]^{2+}$, which is depicted in Figure 6 with respective atomic labels.

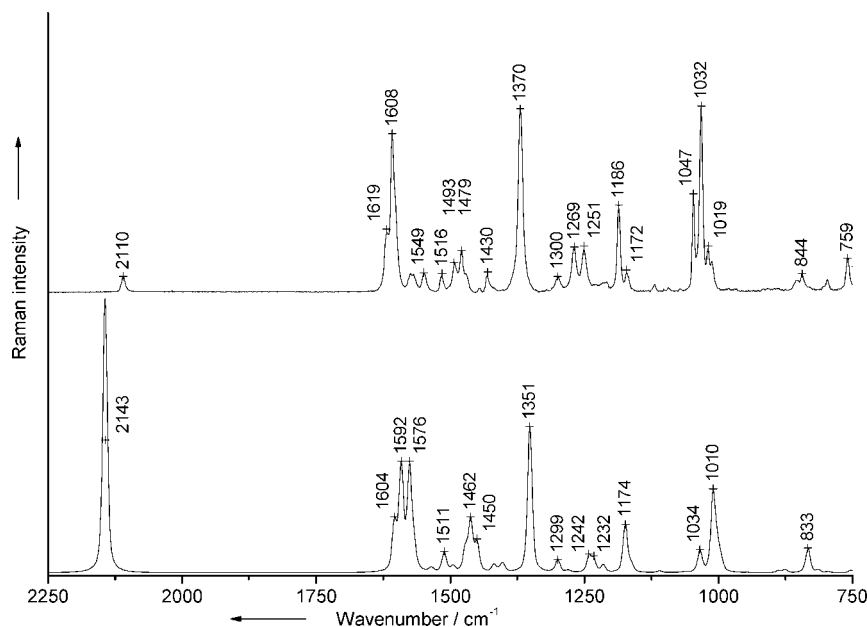


Figure 5. Experimental (top) and DFT calculated (bottom; BP86 functional, def2-TZVP basis set, RI-approximation) Raman spectra of $[\text{Zn}(\text{L})_2]^{2+}$.

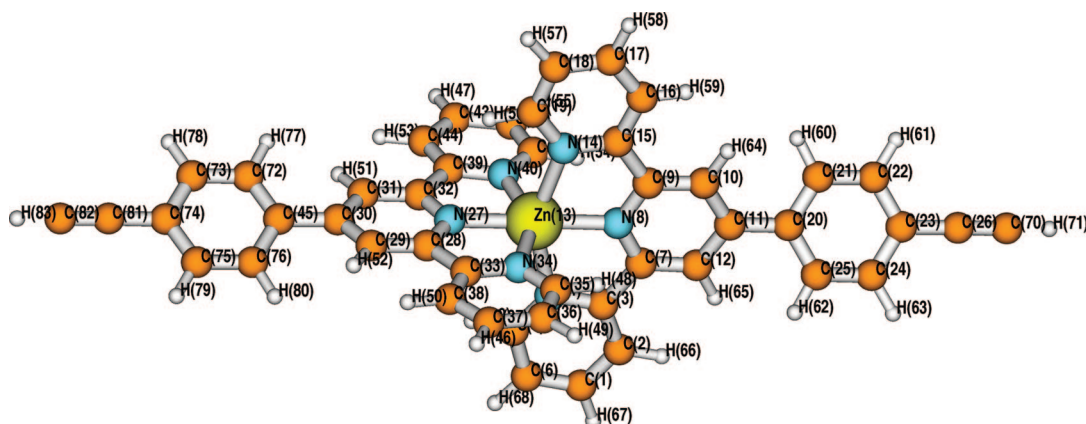


Figure 6. DFT-calculated structure of $[\text{Zn}(\text{L})_2]^{2+}$ with atomic labels.

Tracing the Change of Electron Density Distribution in the ph–py Bond Due to Complexation by Means of Raman Spectroscopy. As previously discussed, changes in the geometry due to complexation, manifested by shortening of the ph–py bond and lowering of the dihedral angle between ph and py, indicate a higher bond order and with it a higher π -character of the ph–py bond. It is possible to monitor these changes by means of Raman spectroscopy since a marker band is present, which involves significant ph–py bond stretchings. This marker band is the trigonal ring breathing mode $\nu(\text{ph–py}(\text{trig}))$ involving strong ph–py bond stretchings and appearing around 1365 cm^{-1} in the experimental RS (see Table 2). It is basically located on the central pyridine ring with strong movements of the substituted carbon atoms. Thus, strong stretchings of the ph–py bond and interpyridine bonds are involved, as shown in the lower graph of Figure 8. An increased bond order due to complexation in the ph–py bond goes along with a higher force constant and is expected to give rise to a shift to higher wavenumbers of $\nu(\text{ph–py}(\text{trig}))$.

When comparing $\nu(\text{ph–py}(\text{trig}))$ between **L** and $[\text{Zn}(\text{L})_2](\text{PF}_6)_2$, one has to account for the 2-fold existence of **L** in the complex $[\text{Zn}(\text{L})_2](\text{PF}_6)_2$. The observed mode coupling leads to a splitting into a symmetric ($\nu(\text{ph–py}(\text{trig}))_s$) and an

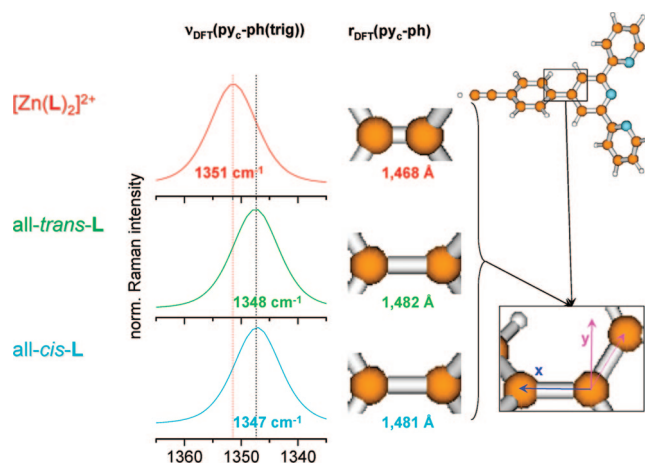


Figure 7. Sketch of the correlation between Raman shift of $\nu(\text{ph–py}(\text{trig}))$ and bond shortening of the ph–py bond upon complexation. Definition of the central pyridine plane: magenta and blue arrows.

asymmetric mode ($\nu(\text{ph–py}(\text{trig}))_{as}$ 180° phase-shifted **L**-vibrations). The symmetric vibration is shifted to higher wavenumbers ($\nu(\text{ph–py}(\text{trig}))_s$: 1351 cm^{-1} , Raman activity 6171

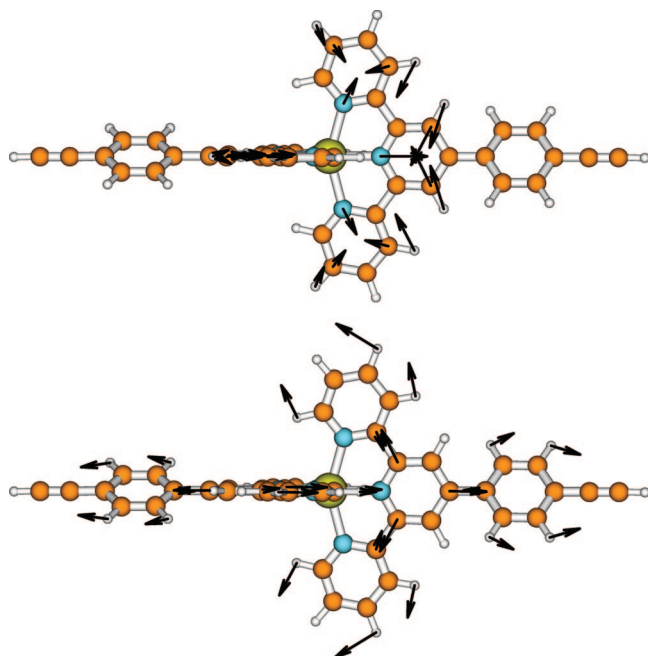


Figure 8. DFT-calculated vibrational pictures of $[\text{Zn}(\text{L})_2]^{2+}$. Top: Trigonal ring breathing mode $\delta_{\text{ip}}(\text{trig. ring br.})$ at 1010 cm^{-1} . Bottom: $\nu(\text{ph-py}(\text{trig}))$ vibration at 1351 cm^{-1} .

$\text{\AA}^4/\text{amu}$), and the asymmetric vibration is shifted to lower wavenumbers ($\nu(\text{ph-py}(\text{trig}))_{\text{as}}$: 1349 cm^{-1} , Raman activity $243 \text{ \AA}^4/\text{amu}$) following our DFT calculations.

In the experimental Raman spectrum of $[\text{Zn}(\text{L})_2](\text{PF}_6)_2$ the band at 1370 cm^{-1} has been assigned to $\nu(\text{ph-py}(\text{trig}))_{\text{s}}$, whereas $\nu(\text{ph-py}(\text{trig}))_{\text{as}}$ exhibits too low intensity to be seen experimentally. The $\nu(\text{ph-py}(\text{trig}))_{\text{s}}$ mode is correlated with the corresponding vibration in **L** $\nu(\text{ph-py}(\text{trig}))$ at 1362 cm^{-1} . So, we have observed a total shift of the $\nu(\text{ph-py}(\text{trig}))$ mode of roughly 8 cm^{-1} when comparing $\nu(\text{ph-py}(\text{trig}))$ of **L** and $[\text{Zn}(\text{L})_2](\text{PF}_6)_2$. This difference exceeds the expected wavenumber shift of 1 cm^{-1} due to splitting of this mode in a symmetric and an antisymmetric mode and hence follows from the higher bond order in the ph-py bond and with it from the increased π -electron delocalization between phenylene and pyridine upon complexation (see Table 2). The correlation between bond length of the ph-py bond and shift of the $\nu(\text{ph-py}(\text{trig}))$ vibration to higher wavenumbers is schematically illustrated in Figure 7.

The higher π -delocalization is further corroborated by the higher calculated Raman activity of $\nu(\text{ph-py}(\text{trig}))_{\text{s}}$ in $[\text{Zn}(\text{L})_2](\text{PF}_6)_2$. This is due to a higher π -character of the ph-py bond, which causes a higher electronic polarizability α and, consequently, a higher Raman activity of $\nu(\text{ph-py}(\text{trig}))$. Together with the Raman activity of $\nu(\text{ph-py}(\text{trig}))_{\text{as}}$, the summed Raman activity is with $6413 \text{ \AA}^4/\text{amu}$ roughly four times higher than for *cis*- and *trans*-**L** (1400 and $1692 \text{ \AA}^4/\text{amu}$, respectively). This finding cannot be explained simply by invoking the 2-fold existence of **L** in $[\text{Zn}(\text{L})_2](\text{PF}_6)_2$ ($2 \times 1692 \text{ \AA}^4/\text{amu} = 3384 \text{ \AA}^4/\text{amu}$) and hence points to an increase of the π -character of the ph-py bond due to complexation. The calculated increase in Raman activity of $\nu(\text{ph-py}(\text{trig}))$ due to complex formation is difficult to confirm experimentally since the two substances exhibit different scattering cross sections. Therefore, the $\nu(\text{ph-py}(\text{trig}))$ Raman band has been normalized to the band of the trigonal ring breathing mode ($\delta_{\text{ip}}(\text{trig. ring br.})$). The vibrational picture of $\nu(\text{ph-py}(\text{trig}))$ as well as of $\delta_{\text{ip}}(\text{trig. ring br.})$ is shown in Figure 8. The $\delta_{\text{ip}}(\text{trig. ring br.})$

mode is mainly located at the terpyridine moiety and thus is assumed to be almost independent of the binding situation in ph-py since it does not involve $\nu(\text{ph-py})$ vibrations.

The quotient of the integrated Raman bands corresponding to $\nu(\text{ph-py}(\text{trig}))$ and to $\delta_{\text{ip}}(\text{trig. ring br.})$ is listed in Table 2. As can be seen, the value corresponding to the Raman data of $[\text{Zn}(\text{L})_2](\text{PF}_6)_2$ (1.35) is roughly twice the value of **L** (2×0.77) confirming the theoretical results ($\text{RA}\{[\text{Zn}(\text{L})_2](\text{PF}_6)_2 - \nu(\text{ph-py}(\text{trig}))_{\text{s+as}}\} = 6413 \text{ \AA}^4/\text{amu}$, $2 \times \text{RA}\{\text{trans-L} - \nu(\text{ph-py}(\text{trig}))\} = 3384 \text{ \AA}^4/\text{amu}$). Thus, the theoretically predicted increase of the Raman activity of $\nu(\text{ph-py}(\text{trig}))$ of $[\text{Zn}(\text{L})_2](\text{PF}_6)_2$ compared to **L** is confirmed experimentally and further evidences the increase of π -character of the ph-py bond in **L** due to complexation. The changes of geometrical parameters upon complexation as well as the Raman shifts and Raman intensity changes are summarized in Table 2. In addition, results of the analysis of the topological properties of the electron density distribution, presented in the next section, are included in Table 2.

Discussion of the Change of Electron Density Distribution in the ph-py Bond Due to Complexation Based on a Topological Analysis and an Intermolecular Electron-Density-Difference Plot. To obtain a more quantitative picture of changes in the degree of π -electron delocalization between phenylene and pyridine due to complexation, an analysis of the DFT-calculated topology of electron density distribution (ρ) according to Bader's AIM theory was performed.^{12a,13} Within this theory, the turning points of the 3-dimensional ρ -distribution are called critical points CP and are classified by the sum over the algebraic signs of the pure partial second derivatives. If in two Cartesian directions maxima and in one Cartesian direction a minimum is present, the critical point is called bond critical point BCP and defines a bond within the AIM theory. The BCPs are located on the so-called surfaces of zero flux (SZF), which includes all trajectories of $\rho(r)$ ending up in the respective BCP and thus dividing the molecule into atoms. By means of the BCP, it is possible to characterize bond properties using particular values enabling a direct comparison or correlation with vibrational and geometrical data. In addition, $\rho(r)$ is an observable, for which reason the resultant calculated properties can be in principle verified experimentally, if high-quality single crystals of the respective substance are available.²⁹ Moreover, the calculated properties of the BCPs are known to be less basis-set dependent, which enables a reliable computation of these properties.³⁰

We have focused on the properties of ρ in the ph-py bond critical point (BCP(ph-py)). The most important features, such as electron density in the BCP itself and corresponding ellipticity (vide infra), are compared in Table 2. Remarkably, ρ differs less between free ligand **L** and the respective complex $[\text{Zn}(\text{L})_2](\text{PF}_6)_2$ in contrast to the ellipticity ε , which is defined as follows (eq 1)

$$\varepsilon = (\lambda_1/\lambda_2) - 1 \quad (1)$$

Herein, $\lambda_{1,2}$ are the two negative curvatures at a BCP, λ_2 being the one with lower magnitude. Since ε in the ph-py-BCP is significantly raised in $[\text{Zn}(\text{L})_2]^{2+}$ to 0.081 as compared to *cis*-**L** (0.069), the assumption of a higher bond order and a higher π -character of the ph-py bond in $[\text{Zn}(\text{L})_2]^{2+}$, based on the geometries and Raman spectra, is supported. As shown in Table 2, ellipticities correlate well with the Raman intensities (RI). However, this behavior cannot be observed for ρ and RI. Unfortunately, the punctiform characterization of the bonding situation in the ph-py bond according to Bader's QTAIM

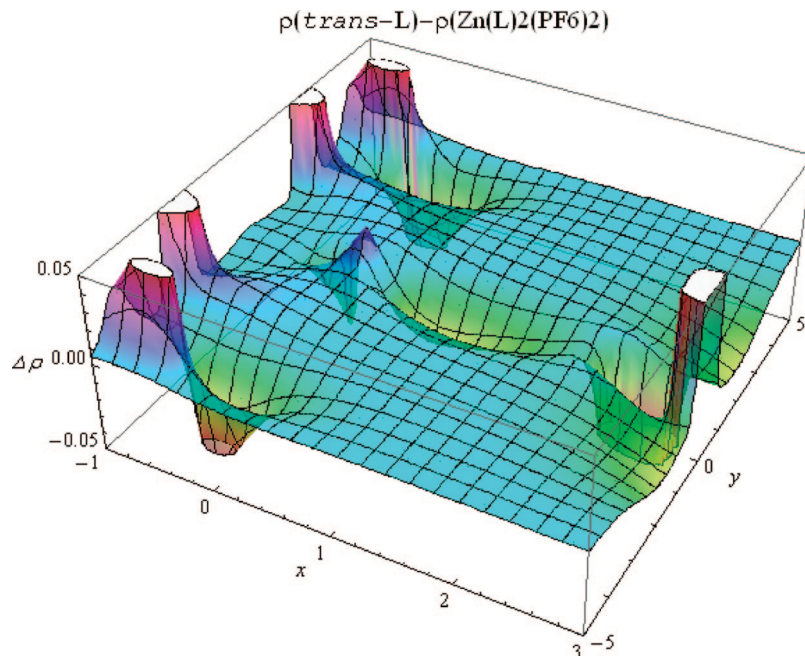


Figure 9. *Inter- $\Delta\rho$* plot: $\rho(\text{trans-L}) - \rho([\text{Zn}(\text{L})_2](\text{PF}_6)_2)$. In the middle of the graph, the ρ difference in the ph-py bond is visible. The origin is the carbon atom belonging to the pyridine ring of the ph-py bond. The vectors defining the drawing plane are depicted in Figure 7. The z-axis corresponds to $\Delta\rho/\text{e}/\text{\AA}^3$. For details, see text.

neither is pictorial nor describes the ph-py bond comprehensively. Hence, we have generated an intermolecular electron-density-difference plot (*inter- $\Delta\rho$* plot) to highlight the changes in the ph-py bond due to complexation (Figure 9).

In this *inter- $\Delta\rho$* plot the ρ -distribution corresponding to the central pyridine plane of $[\text{Zn}(\text{L})_2](\text{PF}_6)_2$ is subtracted from the ρ -distribution of the central pyridine plane in *trans-L*. The plane of the central pyridine rings is defined by the normalized vector corresponding to the ph-py bond and a normalized perpendicular vector lying in the plane of the central pyridine unit and coincides with the drawing plane in Figure 9. These vectors defining the pyridine plane are visualized on the molecular structure graph of **L** in Figure 7, in which the ph-py vector is blue and the second vector defining the py plane is colored magenta. The latter is defined by rotating the vector corresponding to a pyridine carbon-carbon bond (magenta, dotted vector in Figure 7). The atom common to the vectors (C11 in Figure 6) is the origin of the coordinate system. In Figure 9, the molecular section close to the ph-py bond is depicted.

This visualization illustrates changes in the electron density distribution not clearly emerging from ρ -values in the BCP(ph-py). The higher ρ within the ph-py bond of $[\text{Zn}(\text{L})_2](\text{PF}_6)_2$ as compared to **L** is visualized by the valley in the middle of Figure 9. Even the slight electron density fluxes from the central pyridine ring to the ph-py bond upon complexation is revealed by the $\Delta\rho$ plot due to the blue colored positive values along the pyridine-carbon-carbon bonds in Figure 9. The cusps arise from slightly shifted maxima of ρ at positions of the nuclei. In this way, i.e., invoking unscaled atomic distances, also differences in the geometry between $[\text{Zn}(\text{L})_2](\text{PF}_6)_2$ and **L** are visualized. The truncated negative cusp close to the position of the ph-carbon atom in the ph-py bond corresponds to the shortening of the ph-py bond upon complexation.

Hence, this visualization technique facilitates the interpretation of differences in electron density distribution in connection with the geometry of molecular key structures of two different molecules. To compare ρ -distributions of different molecules, it is also possible to plot $\rho(x,y)$ separately for each molecule,

but this is not appropriate to study very small ρ -differences. On the other hand, punctiform tabular comparisons, for example, on the basis of Bader's QTAIM, are neither comprehensive nor illustrative. $\Delta\rho$ plots are predominantly used to study the ρ -distribution of a single molecule as this is the case in deformation density plots.³⁰ In other works, the effect of different orbital constructions or different environments is studied applying $\Delta\rho$ plots.¹⁴ However, the *inter- $\Delta\rho$* plot exhibits a great potential to study ρ - and geometry differences in narrow key regions of two different molecules, as presented in this work and shown by others.¹⁵

Of course *inter- $\Delta\rho$* plots are not applicable to compare larger molecular sections of different molecules since they strongly depend on the respective geometries. To enlarge the molecular section of interest, it is possible to generate the *inter- $\Delta\rho$* plot applying locally equalized geometries to reduce the influence of different nuclear positions. For example, the usage of equalized ph-py bonds is possible by suppressing the normalization of the ph-py corresponding vectors of both molecules and using an equal number of plotting points along the ph-py vector. The (x,y) frame of one of the compared molecules serves as reference, and corresponding ρ -values can be subtracted, which equates to a geometrical adjustment. This technique of matching bond length leads to an improved comparison of electron density regarding spatial more expanded regions. Disadvantageously, this procedure obviously will go along with losing the illustration of changes in the bond lengths between different molecules.

Finally, the investigations of the properties of the electron density distribution, based on Bader's QTAIM and visualized by the *inter- $\Delta\rho$* plot, confirm the assumption of an increased π -character in the ph-py bond due to complexation as already suggested by changes in the geometry and Raman spectra.

Conclusion

In this work, we presented the synthesis and characterization of an ethynylphenyl-substituted terpyridine ligand and its

corresponding zinc(II) complex. Such systems are potentially highly interesting for the construction of PLED or lighting devices. A general question discussed in context with the photophysical and electrochemical properties is the degree of the disturbance of π -electron conjugation between adjacent aromatic rings due to torsion in the case of sterical repulsions. Thus, we focused this study on this particular question. As the bathochrome absorption band of the ligand, assigned to phenyl-localized transitions, is red-shifted due to complexation, we supposed a change in the π -character of the ph–py bond and with it an increase of π -delocalization between the phenylene and the terpyridine moiety. The higher π -character of the ph–py bond in complex $[\text{Zn}(\text{L})_2](\text{PF}_6)_2$ compared to the free ligand was verified by DFT calculations as well as experimental Raman studies. Upon complexation, DFT calculations offered a reduced dihedral angle between ph and py, a shortening of the ph–py bond, and with it a higher wavenumber of the $\nu(\text{ph}–\text{py}(\text{trig}))$ vibration, since it involves strong ph–py bond stretchings, which could be confirmed experimentally. The $\nu(\text{ph}–\text{py}(\text{trig}))$ vibration revealed a significant higher Raman intensity in $[\text{Zn}(\text{L})_2](\text{PF}_6)_2$ than in **L**, which could also be verified experimentally. This correlates well with higher ellipticity in the bond-critical-point of the ph–py bond, according to our QTAIM study, since a higher delocalization corresponds to a higher polarizability. To compare electron density distributions between $[\text{Zn}(\text{L})_2](\text{PF}_6)_2$ and **L** of the ph–py bond key region and the particular adjacent bonds of py, we generated an *inter*– $\Delta\rho$ plot visualizing differences in ρ and in the geometries of these different molecules. Due to the depiction of positive and negative regions, even the shifting of electron density is visualized. Utilizing this visualization technique in conjunction with DFT, Raman, UV–vis, and photoluminescence studies, we are investigating the influence of different *para*-phenylene substituents on the photophysical properties of derived zinc(II) complexes. Within this context also, the influence of the substituents on the terpyridine–phenylene– π -conjugation will be studied. Subsequently, the design of optimized materials for PLED and lighting applications will be targeted.

Acknowledgment. We thank the Dutch Polymer Institute (DPI), the Nederlandse Organisatie voor Wetenschappelijk Onderzoek (NWO, VICI award for U.S. Schubert), the Fonds der Chemischen Industrie, and the Deutsche Forschungsgemeinschaft (Schwerpunktprogramm 1178) for financial support. We also acknowledge Tina Erdmenger and Rebecca Eckardt for performing the MALDI-TOF MS measurements and elemental analysis, respectively. Furthermore, we thank Daniel Escudero for support concerning the AIM2000 program.

Supporting Information Available: Complete vibrational assignment, supported by a DFT calculated Raman spectrum for $[\text{Zn}(\text{L})_2]^{2+}$. This material is available free of charge via the Internet at <http://pubs.acs.org>.

References and Notes

- (1) (a) Lehn, J.-M. *Supramolecular Chemistry, Concepts and Perspectives*; VCH: Weinheim, 1995. (b) Lee, S. J.; Lin, W. J. *Am. Chem. Soc.* **2002**, *124*, 4554–4555. (c) Leininger, S.; Olenyuk, B.; Stang, P. J. *Chem. Rev.* **2000**, *100*, 853–907.
- (2) (a) Schubert, U. S.; Hofmeier, H.; Newkome, G. R. *Modern Terpyridine Chemistry*; Wiley-VCH: Weinheim, 2006. (b) Schubert, U. S.; Eschbaumer, C.; Hien, O.; Andres, P. R. *Tetrahedron Lett.* **2001**, *42*, 4705–4707. (c) Schubert, U. S.; Eschbaumer, C.; Andres, P.; Hofmeier, H.; Weidl, C. H.; Herdtweck, E.; Dulkeith, E.; Morteani, A.; Hecker, N.; Feldmann, J. *Synth. Met.* **2001**, *121*, 1249–1252. (d) Schubert, U. S.; Schmatloch, S.; Precup, A. A. *Des. Monomer Polymer* **2002**, *5*, 211–221.
- (3) (a) Erkkila, K. E.; Odom, D. T.; Barton, J. K. *Chem. Rev.* **1999**, *99*, 2777–2795. (b) Barigelletti, F.; Flamigni, L. *Chem. Soc. Rev.* **2000**, *29*, 1–12. (c) Ott, S.; Kritikos, M.; Åkermar, B.; Sun, L. *Angew. Chem., Int. Ed.* **2003**, *42*, 3285–3288. (d) Heller, M.; Schubert, U. S. *Eur. J. Org. Chem.* **2003**, *6*, 47–61. (e) Andres, P. R.; Schubert, U. S. *Adv. Mater.* **2004**, *16*, 1043–1068. (f) Hofmeier, H.; Schubert, U. S. *Chem. Soc. Rev.* **2004**, *33*, 373–399. (g) Bianké, G.; Häner, R. *ChemBioChem* **2004**, *5*, 1063–1068. (h) Schmitt, M.; Kalsani, V.; Mal, P.; Bats, J. W. *Inorg. Chem.* **2006**, *45*, 6370–6377. (i) Hwang, S. H.; Moorefield, C. N.; Dai, L.; Newkome, G. R. *Chem. Mater.* **2006**, *18*, 4019–4024.
- (4) (a) Barigelletti, F.; Flamigni, L.; Balzani, V.; Collin, J.-P.; Sauvage, J.-P.; Sour, A.; Constable, E. C.; Cargill Thompson, A. M. W. *J. Am. Chem. Soc.* **1994**, *116*, 7692–7699. (b) Barigelletti, F.; Flamigni, L.; Calogero, G.; Hammarström, L.; Sauvage, J.-P.; Collin, J.-P. *Chem. Commun.* **1998**, 2333–2334. (c) Hissler, M.; El-ghayoury, A.; Harriman, A.; Ziessel, R. *Angew. Chem., Int. Ed.* **1998**, *37*, 1717–1720. (d) Bernhard, S.; Goldsmith, J. I.; Takada, K.; Abruña, H. D. *Inorg. Chem.* **2003**, *42*, 4389–4393. (e) Duncan, T. V.; Rubtsov, I. V.; Uyela, H. T.; Therien, M. J. *J. Am. Chem. Soc.* **2004**, *126*, 9474–9475. (f) Barbieri, A.; Ventura, B.; Barigelletti, F.; de Nicolai, A.; Quesada, M.; Ziessel, R. *Inorg. Chem.* **2004**, *43*, 7359–7368. (g) Winter, A.; Egbe, D. A. M.; Schubert, U. S. *Org. Lett.* **2007**, *9*, 2345–2348.
- (5) (a) Chan, C.-W.; Cheng, L.-K.; Che, C.-M. *Coord. Chem. Rev.* **1994**, *132*, 87–97. (b) Whittle, C. E.; Weinstein, J. A.; George, M. G.; Schanze, K. S. *Inorg. Chem.* **2001**, *40*, 4053–4062. (c) Pomestceko, I. E.; Luman, C. R.; Hissler, M.; Ziessel, R.; Castellano, F. N. *Inorg. Chem.* **2003**, *42*, 1394–1396. (d) Adams, C. J.; James, S. L.; Liu, X.; Raitby, P. R.; Yellowless, L. J. *J. Chem. Soc., Dalton Trans.* **2000**, 63–67. (e) Yam, V. W. W. *Acc. Chem. Res.* **2002**, *35*, 555–563. (f) Chan, S.-C.; Chan, M. C. W.; Chan, C. W.; Wang, Y.; Che, C.-M.; Cheung, K.-K.; Zhu, N. *Chem.–Eur. J.* **2001**, *7*, 4180–4190. (g) Ng, W. Y.; Gong, X.; Chan, W. K. *Chem. Mater.* **1999**, *11*, 1165–1170.
- (6) (a) Ziessel, R.; Hissler, M.; El-ghayoury, A.; Harriman, A. *Coord. Chem. Rev.* **1998**, *178–180*, 1251–1298. (b) Balzani, V.; Ceroni, S.; Juris, A.; Venturi, A.; Venturi, M.; Campagna, S.; Puntoriero, F.; Serroni, S. *Coord. Chem. Rev.* **2001**, *219–221*, 545–572. (c) Flood, A. H.; Stoddart, J. F.; Steuerman, D. W.; Heath, J. R. *Science* **2004**, *306*, 2055–2056. (d) Ciofini, I.; Lainé, P. P.; Bedioui, F.; Adamo, C. *J. Am. Chem. Soc.* **2004**, *126*, 10763–10777. (e) Duprez, V.; Biancardo, M.; Spanggaard, H.; Krebs, F. C. *Macromolecules* **2005**, *38*, 10436–10448. (f) Hagemann, O.; Jørgensen, M.; Krebs, F. C. *J. Org. Chem.* **2006**, *71*, 5546–5559. (g) Benniston, A.; Harriman, A.; Li, P.; Patel, P. V.; Sams, C. A. *J. Org. Chem.* **2006**, *71*, 3481–3493.
- (7) (a) Yu, S. C.; Kwok, C. C.; Chan, W. K.; Che, C. M. *Adv. Mater.* **2003**, *15*, 1634–1647. (b) Chang, S. C.; Bharathan, J.; Yang, Y.; Helgeson, R.; Reynolds, J. R. *Appl. Phys. Lett.* **1998**, *72*, 2561–2563. (c) Bliznyuk, V. N.; Carter, S. A.; Scott, J. C.; Klaerner, G.; Miller, R. D.; Miller, D. C. *Macromolecules* **1999**, *32*, 361–369. (d) Xia, C.; Advincula, R. C. *Macromolecules* **2001**, *34*, 5854–5859. (e) Dobrawa, R.; Lysetskaya, M.; Ballester, P.; Grüne, M.; Würthner, F. *Macromolecules* **2005**, *38*, 1315–1325. (f) Chen, Y.-Y.; Tao, Y.-T.; Lin, H. C. *Macromolecules* **2006**, *39*, 8559–8566. (g) Chen, Y.-Y.; Lin, H.-C. *J. Polym. Sci., Part A: Polym. Chem.* **2007**, *45*, 3243–3255.
- (8) (a) Chu, Q.; Pang, Y. *J. Polym. Sci., Part A: Polym. Chem.* **2006**, *44*, 2338–2345. (b) Hwang, S.-H.; Moorefield, C. N.; Wang, P.; Kim, J.-Y.; Lee, S.-W.; Newkome, G. R. *Inorg. Chim. Acta* **2007**, *360*, 1780–1784.
- (9) Chou, P.-T.; Chi, Y. *Chem.–Eur. J.* **2007**, *12*, 380–395.
- (10) (a) Wang, X. Y.; Del Guerso, A.; Schmehl, R. H. *Chem. Commun.* **2002**, 2344–2345. (b) Goodall, W.; Williams, J. A. G. *Chem. Commun.* **2001**, 2514–2515.
- (11) (a) Westenhoff, S.; Beenken, W. J. D.; Friend, R. H.; Greenham, N. C.; Yartsev, A.; Sundstrom, V. *Phys. Rev. Lett.* **2006**, *97*, 166804/1–166804/4. (b) Beenken, W. J. D.; Lischka, H. J. *Chem. Phys.* **2005**, *123*, 144311/1–144311/9. (c) Westenhoff, S.; Beenken, W. J. D.; Yartsev, A.; Greenham, N. C. *J. Chem. Phys.* **2006**, *125*, 154903/1–154903/7. (d) Göller, A. H.; Grummt, U.-W. *Chem. Phys. Lett.* **2002**, *354*, 233–242.
- (12) (a) Bader, R. F. W. *Atoms in Molecules: A Quantum Theory*; Oxford University Press: New York, 1990. (b) Biegler-König, F.; Schönbohm, J. *J. Comput. Chem.* **2002**, *23*, 1489–1494. (c) Volkov, A. V. *MOLDEN2WFN*; Department of Chemistry, Middle Tennessee State University: USA, 2008.
- (13) Bader, R. F. W.; Chang, C. J. *Phys. Chem.* **1989**, *93*, 2946–2956.
- (14) (a) Deepa, P.; Kolaival, P.; Senthikumar, K. *Biophys. Chem.* **2008**, *136*, 50–58. (b) Hensen, C.; Hermann, J. C.; Nam, K.; Ma, S.; Gao, J.; Hölte, H.-D. *J. Med. Chem.* **2004**, *47*, 6673–6680. (c) Absar, I.; Van Wazer, J. R. *Angew. Chem.* **1978**, *90*, 86–95. (d) Gao, J.; Xia, X. *Science* **1992**, *258*, 631–625.
- (15) (a) McRee, D. E.; Redford, S. M.; Getzoff, E. D.; Lepock, J. R.; Hallewell, R. A.; Tainer, J. A. *J. Biol. Chem.* **1990**, *265*, 14234–14241. (b) Monteillet, C.; Blow, D. M. *J. Mol. Biol.* **1978**, *122*, 407–417. (c) Grier, D. L.; Streitwieser, A. *J. Am. Chem. Soc.* **1982**, *104*, 3556–3564.
- (16) Ahlrichs, R.; Bär, M.; Häser, M.; Horn, H.; Kölmel, C. *Chem. Phys. Lett.* **1989**, *162*, 165–169.
- (17) Becke, A. D. *Phys. Rev. A* **1988**, *38*, 3098–3100.

- (18) Perdew, J. P. *Phys. Rev. B* **1986**, *33*, 8822–8824.
- (19) Schäfer, A.; Huber, C.; Ahlrichs, R. *J. Chem. Phys.* **1994**, *100*, 5829–5835.
- (20) (a) Eichkorn, K.; Treutler, O.; Öhm, H.; Häser, M.; Ahlrichs, R. *Chem. Phys. Lett.* **1995**, *240*, 283–290. (b) Eichkorn, K.; Weigend, F.; Treutler, O.; Ahlrichs, R. *Theor. Chem. Acc.* **1997**, *97*, 119–124.
- (21) Neugebauer, J.; Reiher, M.; Kind, C.; Hess, B. A. *J. Comput. Chem.* **2002**, *23*, 895–910.
- (22) Wolfram-Research, Inc., Champaign, Illinois, USA, 2005.
- (23) Constable, E. C.; Lewis, J.; Liptrot, M. C.; Raithby, P. R. *Inorg. Chim. Acta* **1990**, *178*, 47–54.
- (24) Tessore, F.; Roberto, D.; Ugo, R.; Pizzotti, M. *Inorg. Chem.* **2005**, *44*, 8967–8978.
- (25) Ziegler, M.; Monney, V.; Stöckli-Evans, H.; von Zelewsky, A.; Sasaki, I.; Dupic, G.; Daran, J.-C.; Balavoine, G. G. A. *J. Chem. Soc., Dalton Trans.* **1999**, 667–676.
- (26) (a) Herrmann, C.; Neugebauer, J.; Presselt, M.; Schmitt, M.; Rau, S.; Popp, J.; Reiher, M. *J. Phys. Chem. B* **2007**, *111*, 6078–6087. (b) Reiher, M.; Brehm, G.; Schneider, S. *J. Phys. Chem. A* **2004**, *108*, 734–742.
- (27) For related work on transition metal bisterpyridine complexes, see also: (a) Morai, C. *Phys. Lett. A* **2008**, *372*, 1885–1889. (b) Lin, X.; Phillips, D. L. *J. Org. Chem.* **2008**, *73*, 3680–3688. (c) Lundqvist, M. J.; Nilsing, M.; Lunell, S.; Åkermark, B.; Persson, P. *J. Phys. Chem. B* **2006**, *110*, 20513–20525.
- (28) Dollish, F. R. *Characteristic Raman Frequencies of Organic Compounds*; John Wiley & Sons Inc.: New York, 1973.
- (29) (a) Henn, J.; Leusser, D.; Stalke, D. *J. Comput. Chem.* **2007**, *28*, 2317–2324. (b) Luger, P. *Org. Biomol. Chem.* **2007**, *5*, 2529–2540.
- (30) Messerschmidt, M.; Wagner, A.; Wong, M. W.; Luger, P. *J. Am. Chem. Soc.* **2002**, *124*, 732–733.

JP807461J